Journal of Asian Earth Sciences 160 (2018) 107–117

Contents lists available at ScienceDirect

Journal of Asian Earth Sciences

journal homepage: www.elsevier.com/locate/jseaes

Full length article

Prehnite as an indicator mineral in the Wadi Nasb uralitized gabbro, South Sinai, Egypt

Mokhles K. Azer[a,*], Hisham A. Gahlan[b,c], Paul D. Asimow[d], Hussain J. Alfaifi[b]

[a] Geological Sciences Department, National Research Centre, Cairo, Egypt
[b] Department of Geology and Geophysics, King Saud University, Riyadh 11451, Saudi Arabia
[c] Geology Department, Assiut University, Assiut 71516, Egypt
[d] Division of Geological & Planetary Sciences, California Institute of Technology, USA

ARTICLE INFO

Keywords:
Arabian-Nubian Shield
Sinai
Appinitic gabbro
Uralitization
Prehnite

ABSTRACT

We report the first finding of prehnite in the southern Sinai peninsula, in a uralitized gabbro developed at the contact of the appinitic gabbro of the Wadi Nasb mafic intrusion (WNMI) with younger granitic intrusions. Subsolidus reactions with hydrothermal fluids caused the gabbro to gain Al_2O_3 and CaO while losing SiO_2, Fe_2O_3, TiO_2, P_2O_5, Ba, Nb, Zr and Y. Uralitization proceeded through two stages of alteration and mineral replacement. The early stage includes uralitization of pyroxene, formation of new biotite as aggregates of small flakes, transformation of primary amphiboles into actinolite and actinolitic hornblende, and saussuritization of plagioclase. The late stage of alteration is characterized by chloritization of mafic minerals. Apparent crystallization temperatures of the primary relics of pyroxene, hornblende and biotite range from 800–1000 °C, 865–925 °C, and ~700 °C, respectively, suggesting partial resetting of the biotite exchange thermometer. The early biotite-forming alteration occurred at moderate temperature (300–450 °C), while the late chlorite-forming alteration occurred at low temperature (< 300 °C). The prehnite occurs in several forms: (1) fine grained aggregates mostly replacing feldspar and amphibole; (2) prehnite-biotite intergrowths; and (3) small veinlets and vug fillings. The formation of prehnite during the first stage is connected to alteration of pyroxene to secondary amphiboles and of plagioclase to albite, which released the CaO necessary for the development of prehnite. On the other hand, the late stage prehnite probably formed by open-system modification of the chemistry during late-stage fluid interaction.

1. Introduction

The Wadi Nasb mafic intrusion (WNMI), southern Sinai, Egypt, is a generally undeformed and unmetamorphosed appinitic (primary hornblende-bearing) gabbro. Its hornblende-bearing character is unique among the post-collisional mafic magmatic rocks of the northern Arabian-Nubian Shield (ANS) (Gahlan et al., 2018). The WNMI has been well-studied from the point of view of its primary petrological and mineralogical variations in a series of papers focused on its origin and tectonic setting (Soliman, 1996; Abdel-Karim, 2013; Samuel et al. 2015; Gahlan et al., 2018). Although selected samples of uralitized gabbro from the margin of the WNMI were petrographically described by Gahlan et al. (2018), no bulk chemical analyses have been published and no previous work has focused on alteration products of the WNMI or other mafic intrusions in south Sinai.

Indeed, the published descriptions of the WNMI are apparently contradictory concerning alteration associated with the intrusion. Some previous studies did not report any uralitized gabbro associated with the WNMI (Soliman, 1996; Samuel et al. 2015). On the other hand, Abdel-Karim (2013) considered the entire gabbroic mass of the WNMI to be uralitized gabbro and hornblendite emplaced in the final arc stage of an active continental margin. However, the recent work by Gahlan et al. (2018) indicates that the uralitized gabbro is restricted to minor exposures along the margins of the WNMI, adjacent to later granitic intrusions, and that hornblendite occurs only as a thin screen where emplacement of the WNMI produced greenschist-facies metamorphism of the adjacent metasediments (Gahlan et al., 2018).

This study examines the origin of the uralitized gabbro along the margin of the WNMI on the basis of detailed field, petrographical, mineralogical and geochemical studies. We report, for the first time, the occurrence of prehnite in south Sinai. Prehnite, most often found as a late-stage mineral formed by hydrothermal alteration of mafic intrusions (e.g. Cairncross et al., 2000), has been recorded in the Eastern Desert of Egypt where granitic intrusions interacted with pre-existing

* Corresponding author.
E-mail address: mk.abdel-malak@nrc.sci.eg (M.K. Azer).

https://doi.org/10.1016/j.jseaes.2018.04.011
Received 2 November 2017; Received in revised form 10 April 2018; Accepted 13 April 2018
Available online 14 April 2018
1367-9120/

gabbro (Essawy and Hassan, 1977). Here, we provide detailed textural observations, whole-rock compositions of the uralitized gabbro, and compositions of the associated prehnite and other secondary minerals. These results support a discussion of the element mobility during the uralitization process, the subsolidus history of the intrusion and its hydrothermal alteration, and the formation conditions of various textures of prehnite.

2. Geology

The Precambrian basement outcrops of the Eastern Desert and Sinai constitute the northern part of the Nubian Shield, which was contiguous with the Arabian shield on the Arabian Peninsula before the opening of the Red Sea; together these form the ANS. A number of Late Neoproterozoic mafic plutons intrude the juvenile crust of the ANS in south Sinai. Some synorogenic intrusions are deformed and variably metamorphosed (e.g. Moussa, 1999; Mehanna et al., 2004; Azer et al., 2016), whereas those considered to be post-orogenic are quite fresh, undeformed and unmetamorphosed (e.g. Azer and El-Gharbawy, 2011; Azer et al., 2012, Khalil et al. 2015, Gahlan et al., 2018).

The WNMI is one of many late Neoproterozoic mafic intrusions in south Sinai, including the Tweiba, Nakhil, El-Mahash, Sa'al-Zaghra, Imleih, Nasrin, Rimm, Hibran-Mi'ar, Nasb, Imlaha and Shahira intrusions (Fig. 1a). Detailed field studies of the WNMI (Soliman, 1996; Abdel-Karim, 2013; Samuel et al., 2015; Gahlan et al., 2018) have established that it sits outside the southern sector of the Katherina Ring complex as an undeformed oval-shaped intrusion. It intrudes syn-tectonic calc-alkaline rocks and in turn is truncated by post-collisional calc-alkaline and alkaline granites (Fig. 1b). The crystallization age of the WNMI has not been measured directly, but the intrusive relations and available geochronological data for other nearby rocks bound its age to 619–610 Ma (Gahlan et al., 2018). Based on the field relations, the WNMI was emplaced in a post-collisional environment.

Detailed geochemical characterization of the fresh rocks of the WNMI is given by Samuel et al. (2015) and Gahlan et al. (2018). The WNMI is mostly medium-K calc-alkaline in nature with continuous linear composition trends in all major and trace element variation diagrams, suggesting a co-genetic origin for the whole intrusion (Gahlan et al., 2018). A quantitative fractionation model of the WNMI suggests evolution was controlled by fractional crystallization of an assemblage of 61% primary amphibole, 10% clinopyroxene, 28% plagioclase, 1% biotite, 0.4% apatite, and 0.15% Fe-Ti oxide (Gahlan et al., 2018). The appinitic character of the WNMI, with very early hornblende crystallization, points to the fundamental role of water during its generation, differentiation, and emplacement.

As noted by Gahlan et al. (2018), the WNMI interacted with later granitic intrusions at the depth of granite emplacement. This interaction resulted in the alteration of appinitic gabbro into uralitized gabbro and the development of secondary minerals including prehnite. The high-temperature stages of this contact metamorphism likely occurred at ~610 and 599 Ma, the crystallization ages of the calc-alkaline and alkaline granites, respectively (Be'eri-Shlevin et al. 2009; Moreno et al. 2012). Our field observations indicate that thermal metamorphism varied in intensity with distance from granitic intrusions and with fracture density in the pluton; the localization of severe alteration in highly fractured parts of the pluton suggests that the fractures predate the alteration and provided fluid infiltration conduits. Gahlan et al. (2018) only reported uralitized gabbro on the northern margin of the WNMI, at the contact with the monzogranite of G. Nakhila. Our additional field observations document uralitized gabbro at three further sites on the southern margin of the WNMI, at contacts with the Rahba granite (Fig. 1b). At each locality, a thin outcrop region (~20 to 150 cm) of uralitized gabbro grades into fresh appinitic gabbro. Each uralitized gabbro location was sampled for petrographic and geochemical investigation.

3. Petrography

Previous authors divided the rocks of the WNMI into appinitic gabbro, fine-grained gabbro and uralitized gabbro (Samuel et al., 2015; Gahlan et al., 2018) and provided petrographic description of each type. Here, we expand specifically on the description of uralitized gabbro based on thin sections of more than 50 samples.

In the uralitized gabbro, primary amphiboles are extensively replaced by secondary green amphibole, plagioclase is highly altered, clinopyroxene is partly to completely replaced by actinolite and chlorite, and biotite shows various degrees of alteration. Although primary minerals are highly altered, the original texture is preserved and fresh relics of all the primary minerals can be found. The secondary mineral assemblages include actinolite, actinolitic hornblende, albite, biotite, prehnite, chlorite, titanite and epidote. These minerals appear to have been formed in more than one generation. Primary amphibole occurs as brown cores within secondary green amphibole, easily distinguished by color and pleochroism. Plagioclase occurs as highly altered tabular crystals, replaced mainly by albite along crystal margins and by prehnite and epidote in the cores (Fig. 2a). A few fresh relics of plagioclase with original concentric zoning were observed in some thin sections. Vugs filled by nests of secondary albite are also found (Fig. 2b).

Most clinopyroxene grains show peripheral alteration to uralite and actinolite or actinolitic hornblende (Fig. 2c). Some relics of clinopyroxene are entirely surrounded by feathery chlorite. In many cases, isolated clinopyroxene remnants within chlorite patches show simultaneous optical extinction, demonstrating that they were parts of large, single clinopyroxene crystals, now almost entirely chloritized. Both magmatic and secondary biotites are observed. The primary, magmatic biotite occurs as fresh dark brown relics showing all stages of alteration to chlorite, Fe-Ti oxides, and prehnite (Fig. 2d). The secondary biotite commonly occurs as anhedral, light brown to green fine-grained aggregates and flakes, replacing magmatic hornblende. Locally, biotite cleavages bend around prehnite crystals. Some crystals of primary amphibole are recrystallized into aggregates of actinolite, biotite and chlorite forming decussate texture (Fig. 2e), commonly considered a hallmark of contact metamorphism (Azer, 2007). Rarely, ilmenite is rimmed by titanite.

Prehnite appears colorless, a characteristic of the iron-poor varieties (Matsueda, 1975). On textural grounds, two generations of prehnite can be distinguished. Type I occurs as fine-grained aggregates or irregular masses associated with other alteration products (Fig. 2f) or intergrown with biotite (Fig. 2d). Type II locally replaces albite and grew around the early formed epidote or fills cavities with fan-shaped crystals (Fig. 2 g). Type II is distinctively free of inclusions. Epidote occurs as clusters of euhedral prisms in areas interstitial to other phases (Fig. 2 h), in variable quantities as vein fillings, and as a replacement product in the cores of altered plagioclase and biotite.

4. Methods

Electron microprobe analyses of mineral phases in the uralitized gabbro were acquired using a five-spectrometer JEOL JXA-8200 electron microprobe at the Geological and Planetary Sciences (GPS) Division Analytical Facility, California Institute of Technology, USA. Operating conditions were 15 kV accelerating voltage, 25nA beam current, a focused beam (1 μm), 20 s on-peak and 10 s off-peak counting times, and a mix of natural and synthetic mineral standards. Matrix correction was performed using the CITZAF routine. All electron microprobe data are given in the Supplementary Tables (S1–S8).

Whole-rock major and trace elements were determined by X-ray fluorescence (ThermoARL XRF Spectrometer) at the GeoAnalytical Lab, Washington State University, USA. The X-ray conditions were 60 milliamps, 60 kV and a 29 mm aperture. Powdered samples were weighed, mixed with two parts di-lithium tetraborate flux to one part rock

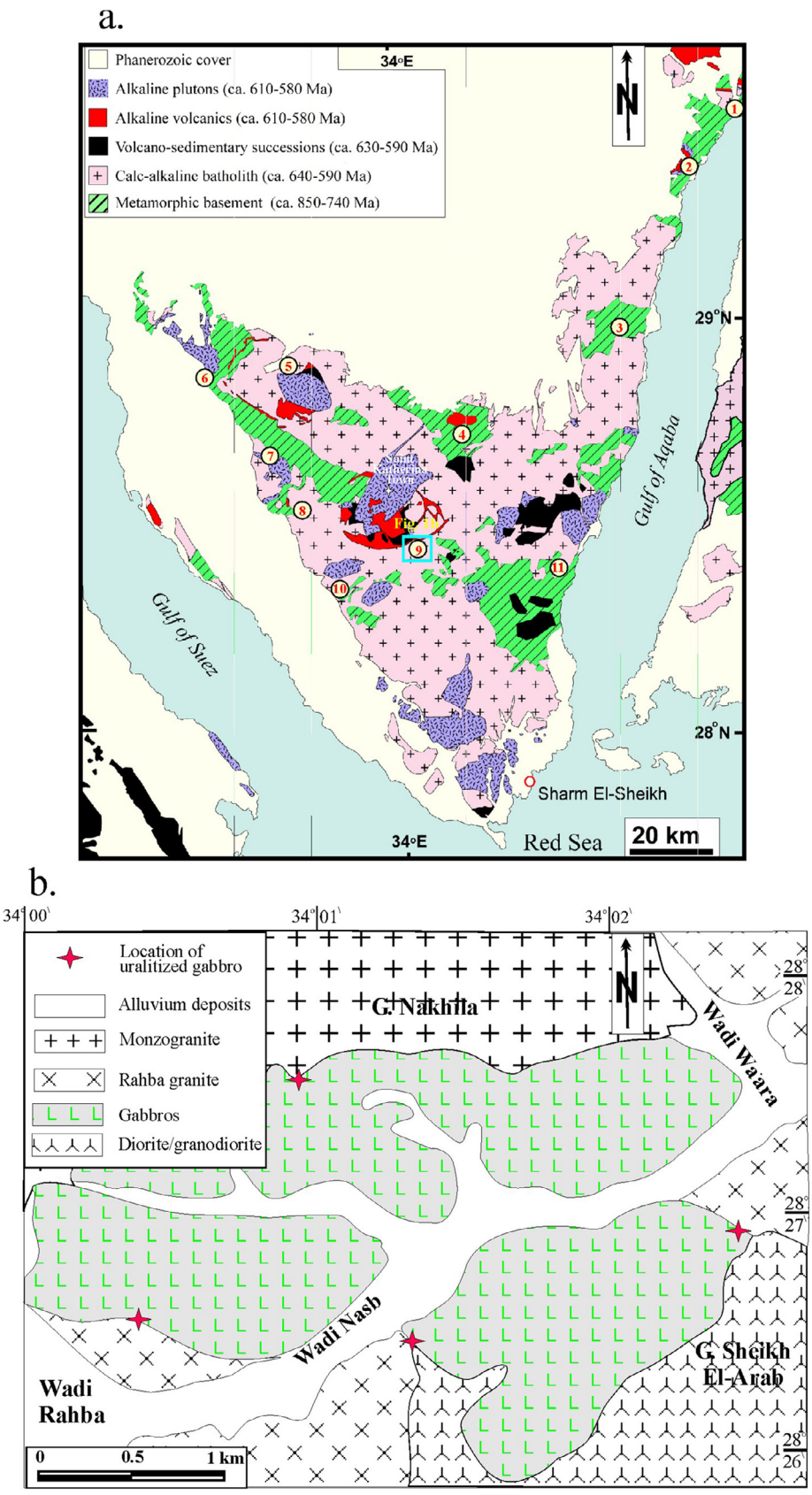

Fig. 1. (a) Geological map of Sinai Peninsula (modified after Be'eri-Shlevin et al., 2011). Location of the study area displayed in Fig. 1b is marked by light blue box. Eleven late Neoproterozoic mafic intrusions in Sinai are indicated: (1) Tweiba, (2) El-Mahash, (3) Nakhil, (4) Sa'al-Zaghra, (5) Imleih, (6) Nasrin, (7) Rimm, (8) Hibran-Mi'ar, (9) Nasb (the present work), (10) Imlaha and (11) Shahira intrusions. (b) Geologic map of Wadi Nasb area (modified after Eyal et al. 2013), with uralitized gabbro sites indicated.

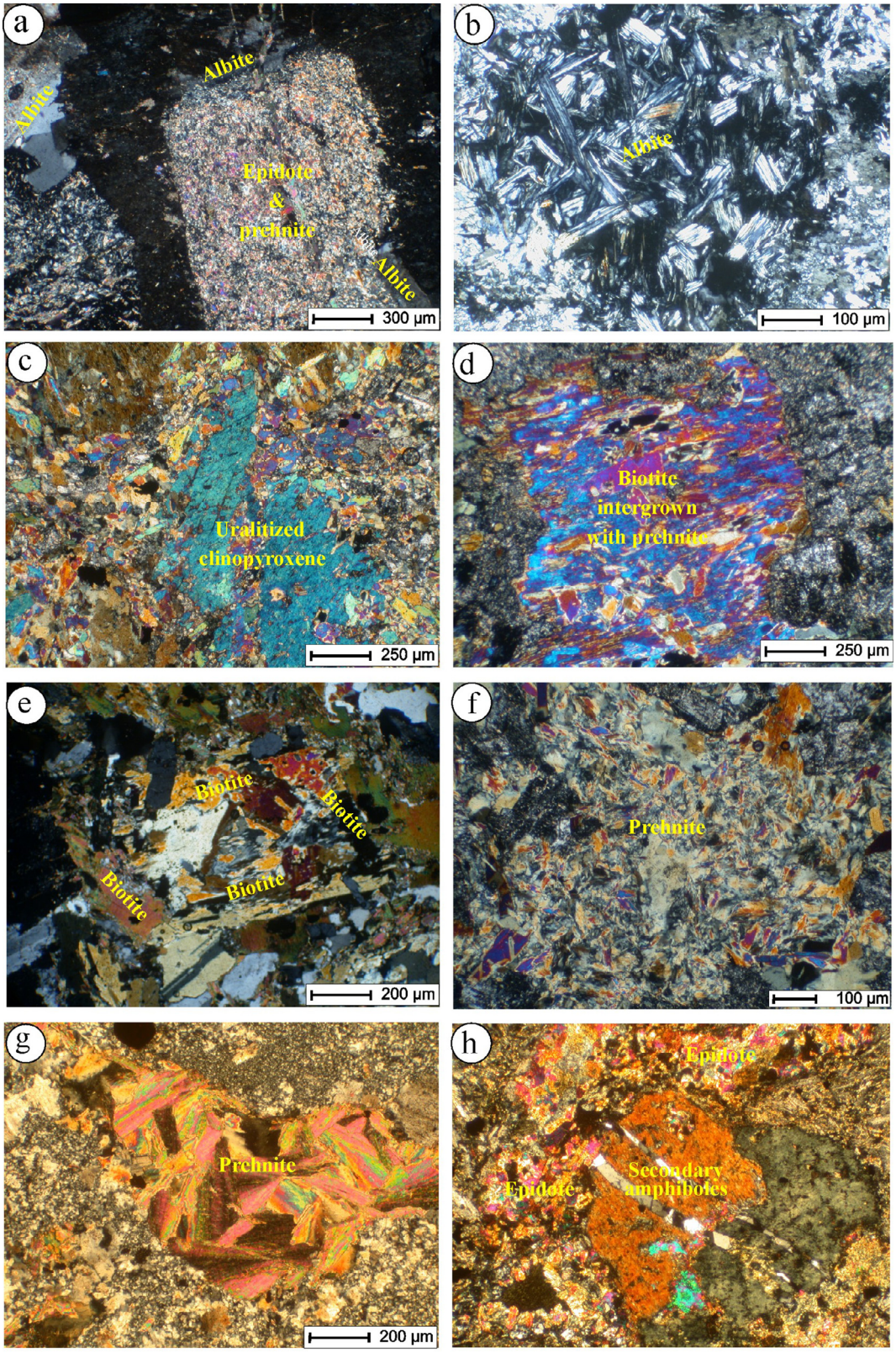

Fig. 2. Photomicrographs showing textures and mineral characteristics of uralitized gabbro: (a) highly altered plagioclase crystals with development of prehnite plus epidote core and albitized rims, (b) vug-filling nests of albite, (c) uralitized clinopyroxene, (d) highly altered biotite with development of prehnite, (e) decussate texture after hornblende, (f) fine-grained aggregates of prehnite, (g) fan-shaped prehnite crystals filling a vug, and (h) clusters of epidote interstitial to other constitute.

Table 1
Major, trace and REE element contents of the uralitized gabbro and averages of fresh gabbros of Wadi Nasb mafic intrusion (WNMI).

Rock type	Uralitized gabbro							Averages			Detection limits	Standard GSP2
Sample No.	U-10	U-11	U-12	U-13	U-R14	U-R16	U-R19	1*	Fresh appinitic gabbro			
									2**	3***		
Major oxides (wt.%)												
SiO2	47.03	47.33	46.72	46.92	46.44	47.21	47.25	46.99	49.12	47.14	0.58	65.92
TiO2	0.41	0.47	0.51	0.55	0.43	0.54	0.61	0.50	0.53	0.40	0.017	0.662
Al2O3	16.78	16.91	16.75	16.85	17.31	16.63	17.77	17.00	16.64	16.85	0.16	14.67
Fe2O3	9.55	9.27	9.68	9.06	7.67	7.02	7.76	8.57	8.13	8.45	0.20	4.46
MnO	0.19	0.21	0.22	0.24	0.18	0.17	0.17	0.20	0.17	0.18	0.002	0.041
MgO	6.48	6.08	6.22	6.52	8.32	8.35	8.17	7.16	8.09	8.47	0.076	0.95
CaO	12.25	12.71	12.76	13.24	12.56	13.05	11.21	12.54	11.16	12.13	0.064	2.08
Na2O	2.09	1.93	1.94	2.01	2.33	2.13	2.18	2.09	1.96	1.18	0.045	2.71
K2O	0.68	0.66	0.71	0.63	0.96	1.03	0.81	0.78	1.19	1.44	0.031	5.40
P2O5	0.21	0.23	0.23	0.25	0.14	0.21	0.13	0.20	0.26	0.22	0.005	0.277
LOI	3.45	3.68	3.41	3.61	3.58	3.44	3.53	3.53	2.59	3.23	–	–
Total	99.12	99.48	99.15	99.88	99.92	99.78	99.59	99.56	99.83	99.69	–	97.17
Trace elements (ppm)												
Ni	57	65	58	63	73	62	59	62.4	70.0	78.0	3.5	16
Cr	252	261	248	256	254	263	250	254.9	236.9	257.5	3.0	19
Sc	36	32	39	40	37	35	35	36.3	37.5	–	1.6	6
V	164	175	186	178	164	167	159	170.4	186.1	226.8	5.0	51
Ba	268	287	259	263	284	323	276	280.0	290.5	308.2	11.7	1329
Rb	49	57	54	60	48	57	52	53.9	49.6	38.0	1.7	246
Sr	487	505	491	511	506	518	477	499.3	565.6	505.2	4.6	242
Zr	45	51	48	50	31	38	41	43.4	43.1	30.7	3.9	555
Y	11	10	9	12	10	11	9	10.3	11.2	7.3	1.2	26
Nb	3.4	3.1	4.2	3.2	1.3	1.6	2.8	2.8	3.3	2.8	1.2	27.6
Ga	12.4	13.2	12.5	12.7	12.2	11.8	11.5	12.3	15.3	13.2	2.7	22
Cu	54	60	58	71	48	61	56	58.3	73.8	–	7.4	46
Zn	52	92	87	96	74	71	91	80.4	79.5	–	3.3	118
Pb	9	8	11	12	7	8	13	9.7	8.8	–	2.6	40
Th	1.77	1.8	1.2	0.9	0.6	0.7	0.5	1.1	1.5	–	1.6	111
U	0.7	0.8	0.6	1.4	0.5	0.6	0.9	0.8	0.6	–	2.7	1
REE (ppm)												
												STD SO-18
La	–	4.56	4.01	–	3.53	5.39	–	–	6.50	6.93	0.1	12.4
Ce	–	9.18	8.97	–	8.09	12.82	–	–	15.02	15.63	0.1	27.9
Pr	–	1.29	1.15	–	0.98	1.56	–	–	1.96	2.12	0.02	3.36
Nd	–	5.74	5.41	–	4.44	6.96	–	–	8.72	9.60	0.3	14.0
Sm	–	1.63	1.44	–	1.26	1.92	–	–	2.47	2.51	0.05	2.86
Eu	–	0.61	0.56	–	0.49	0.68	–	–	0.91	0.83	0.02	0.86
Gd	–	1.78	1.59	–	1.38	2.06	–	–	2.65	2.57	0.05	2.95
Tb	–	0.28	0.25	–	0.23	0.36	–	–	0.43	0.43	0.01	0.49
Dy	–	1.68	1.58	–	1.44	2.16	–	–	2.65	2.47	0.05	2.94
Ho	–	0.35	0.32	–	0.29	0.46	–	–	0.56	0.51	0.02	0.61
Er	–	1.02	0.91	–	0.8	1.22	–	–	1.59	1.49	0.03	1.81
Tm	–	0.15	0.14	–	0.12	0.19	–	–	0.24	0.22	0.01	0.27
Yb	–	1.04	0.95	–	0.85	1.31	–	–	1.62	1.37	0.05	1.78
Lu	–	0.15	0.14	–	0.13	0.18	–	–	0.22	0.17	0.01	0.27
Geochemical ratios												
Eu/Eu*	–	1.09	1.13	–	1.14	1.04	–	–	1.09	0.99	–	–
(La/Yb)n	–	2.97	2.85	–	2.81	2.78	–	–	2.72	3.43	–	–
(La/Sm)n	–	1.77	1.76	–	1.77	1.77	–	–	1.66	1.74	–	–
(Gd/Lu)n	–	1.45	1.39	–	1.30	1.40	–	–	1.50	1.89	–	–
(Ce/Yb)n	–	2.29	2.45	–	2.47	2.53	–	–	2.40	2.96	–	–
(La/Lu)n	–	3.11	2.93	–	2.78	3.07	–	–	3.07	4.26	–	–

Average-1* = the present work.
Average-2** = Gahlan et al. (2018).
Average-3*** = Samuel et al. (2015).

powder, fused at 1000 °C in a muffle oven, and cooled. Each bead was then reground, refused, and polished on diamond laps to provide a smooth and flat surface for analysis. Calibration was based on international standard GSP2; our analysis of the standard is included in Table 1. The internal precision for XRF analyses, calculated from duplicate samples, is better than 1% for most major elements and better than 5% for most trace elements (except Ni, Cr, Sc and V).

The REE were analyzed at ACME Analytical Laboratories (Canada) using Inductively Coupled Plasma Mass Spectrometry (ICP-MS) following lithium metaborate/tetraborate fusion and nitric acid digestion of 0.2 g samples. The analytical precision and detection limits for ACME analyses are listed on the laboratory website (http://acmelab.com/services/method-descriptions) and we provide the analysis of accepted geostandard reference material SO-18 in Table 1.

5. Mineral chemistry

Microprobe analyses of the constituent mineral phases of uralitized

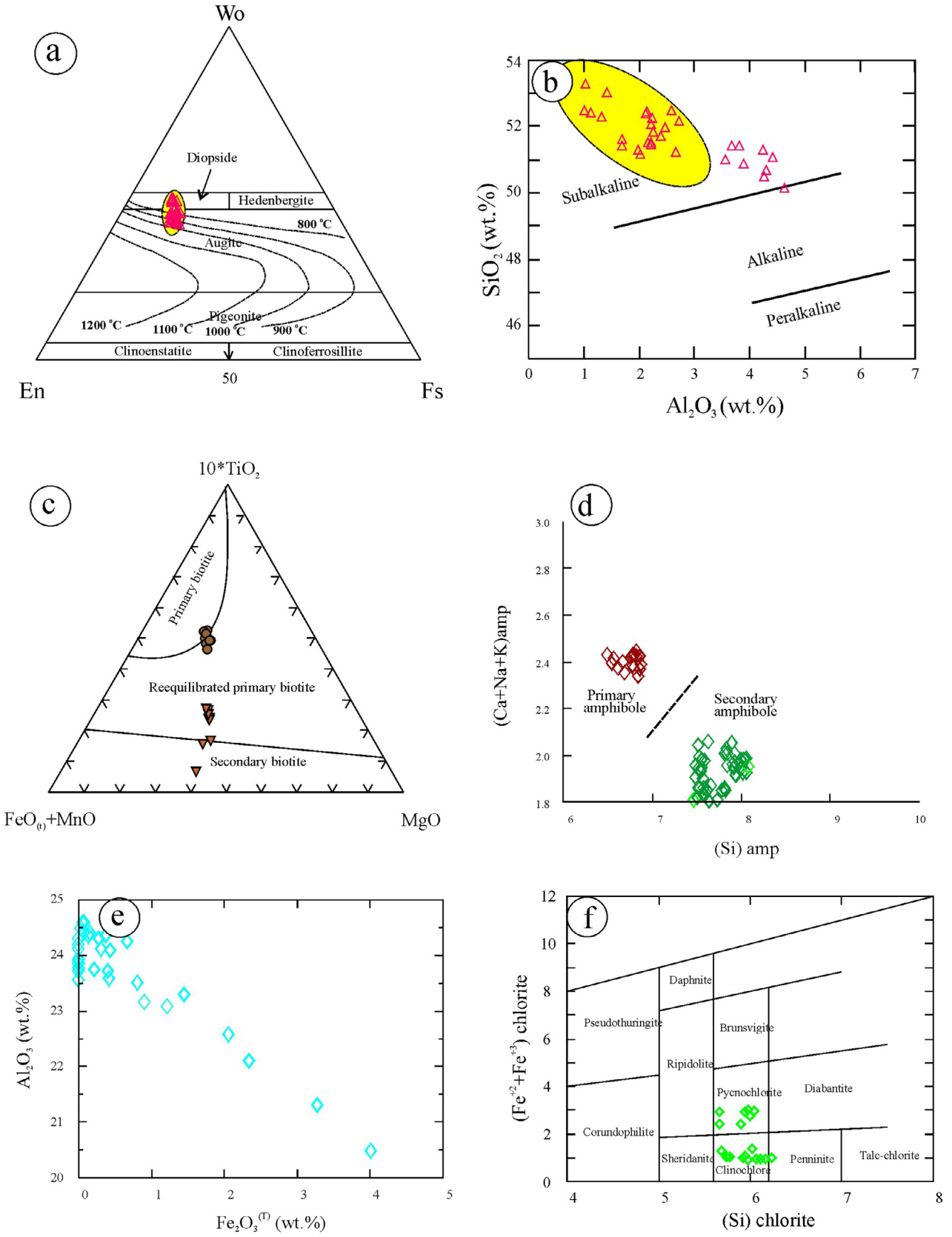

Fig. 3. Mineral chemistry from the WNMI uralitized gabbro. Yellow fields indicate range of analyses in fresh appinitic gabbro from the WNMI after Gahlan et al. (2018). (a) Classification diagram of the analyzed pyroxenes (after Morimoto et al, 1988) with isotherms after Lindsley (1983). (b) SiO_2-Al_2O_3 discrimination diagram of clinopyroxene (after Le Bas, 1962). (c) TiO_2-($FeO_{(t)}$ + MnO)-MgO ternary diagram for classification of biotite (after Nachit et al. 2005). (d) Discrimination diagram for the primary and secondary amphiboles (after Keeditse et al., 2016). (e) $Fe_2O_{3(T)}$ versus Al_2O_3 for prehnite. (f) Chlorite nomenclature (after Hey, 1954). (For interpretation of the references to color in this figure legend, the reader is referred to the web version of this article.)

gabbro, including primary and secondary minerals, are reported in Supplementary Tables S1–S8 and distinctive trends in the compositional of each mineral are described below.

5.1. Pyroxene

Pyroxene is found in uralitized gabbro only as isolated remnants surrounded by secondary amphiboles and chlorite. Chemical compositions and calculated structural formulae of pyroxene are given in Supplementary Tables S1. All relict pyroxenes are rich in CaO, are classified as augite and diopside using the diagram of Morimoto et al. (1988) (Fig. 3a), plot in the subalkaline field of Le Bas (1962) (Fig. 3b), and are mostly indistinguishable from clinopyroxene compositions observed in the fresh appinitic gabbro of the WNMI (Gahlan et al., 2018).

5.2. Biotite

Both dark brown magmatic biotite and greenish-brown secondary biotite were analyzed (Supplementary Table S2). Primary biotite is rich in TiO_2 and K_2O and depleted in Al_2O_3 and MgO compared to secondary biotite. The dark brown magmatic biotite has less than one atom of octahedral Al^{VI} per formula unit (apfu), whereas re-equilibrated and secondary biotite always has high Al^{VI} (Nachit et al., 2005). In the TiO_2-(FeO + MnO)-MgO chemical classification plot of Nachit et al. (2005), the fresh biotite plots in the field of primary biotite, while the biotite after amphiboles in the decussate texture lies mostly in the fields of re-equilibrated primary or secondary biotite (Fig. 3c).

5.3. Amphibole

Microprobe analyses and calculated structural formulae of amphibole-group minerals in the uralitized gabbro (Supplementary Table S3) are quite variable both within and between samples. Rare, brown relics of fresh primary amphibole have high TiO_2 content (> 1.0 wt%), whereas the more common secondary amphibole has low TiO_2 content (< 0.5 wt%). All the amphiboles are rich in CaO (10.8–12.7 wt%) and are classified as calcic amphibole according to the scheme of Leake et al. (1997). Primary amphibole includes magnesio-hornblende and tschermakitic hornblende, whereas secondary amphibole includes actinolite, actinolitic hornblende and uralite.

There is a continuous decrease in Ti, Na, K, and tetrahedral Al^{IV} content from primary to secondary amphibole. The discrimination diagram proposed by Keeditse et al. (2016) for separating magmatic and post magmatic amphibole [Si apfu versus (Ca + Na + K) apfu] fully confirms the assignment of primary and secondary amphiboles by color and texture (Fig. 3d).

5.4. Plagioclase

Most feldspar in the uralitized gabbro is altered, although there are some fresh relics with original concentric zoning. Chemical compositions and calculated structural formulae of feldspar are given in Supplementary Table S4. The plagioclase in uralitized gabbro is mainly albite ($An_{0.94-2.4}$) with lesser oligoclase ($An_{17.9-27.4}$) and andesine ($An_{33.0-50.0}$). The fresh relics are Ca-rich plagioclase ($An_{75.4-82.8}$) in the same range as plagioclase elsewhere in the WNMI (Gahlan et al., 2018). Rare K-feldspar (Or_{93-94}) crystals were recorded in a few samples of uralitized gabbro only.

5.5. Prehnite

The two textural types of prehnite distinguished above were both analyzed. Microprobe analyses of prehnite reveal typical chemical compositions in terms of SiO_2, Al_2O_3 and CaO values with very low TiO_2, MgO, Na_2O and MnO (Supplementary Table S5). The only significant compositional variation observed in prehnites is Fe content, reported here as $Fe_2O_3^T$. Each analyzed prehnite crystal is homogeneous within analytical uncertainty, but different crystals display a range of Fe/Al ratios and a good negative correlation between $Fe_2O_3^T$ and Al_2O_3 (Fig. 3e). This is consistent with the ready substitution of Fe^{3+} and Al^{3+} for one another in the prehnite structure. The maximum iron content is found in type II prehnite, associated with epidote.

5.6. Chlorite

Chlorite is an alteration product of ferromagnesian minerals (including amphibole, pyroxene and biotite) in the WNMI. The chemical composition of chlorite and structural formulae calculated on the basis of 28 oxygens are presented in Supplementary Table S6. All the analyzed chlorites are relatively Mg-rich, with molar Fe/(Fe + Mg) ratios from 0.09 to 0.35. Ti, K and Na are not important constituents in clean, single-phase chlorite analysis spots, but calcium occurs at significant concentrations (0.202–0.209 apfu) in a few analyses. Bettison and Schiffman, (1988) argue that chlorite can accommodate only a minor amount of Ca in its structure and therefore analyses with Ca greater than 0.10 apfu likely indicate the presence of an interlayer smectite component. Adopting the nomenclature scheme of Hey (1954), Fig. 3f, most analyzed chlorite is clinochlore, with an Fe-rich subset classified as pycnochlorite.

The composition of chlorite appears to be controlled by conditions of local equilibrium and by the composition of the primary minerals. Chlorite after amphibole and pyroxene is low in Fe. Chlorite after biotite, sometimes associated with prehnite, has high Al and Fe contents. Mn, Ti and K may appear in these analyses, probably reflecting contamination by incompletely replaced biotite.

5.7. Fe-Ti oxides

The analyzed Fe-Ti oxides (Supplementary Table S7) include magnetite, ilmenite and hematite. Based on TiO_2 contents, magnetite is divided into pure magnetite (TiO_2 < 0.8 wt%) and titanomagnetite (TiO_2 = 18.4–19.6 wt%). The presence of titanomagnetite is confirmed petrographically by the presence of fine trellis intergrowths in magnetite as the result of oxidation of previously exsolved ulvöspinel (Basta, 1960; Buddington and Lindsley, 1964). A few magnetite analyses contain appreciable Cr_2O_3 (up to 1.5 wt%).

Ilmenite is richer in MnO (2.2–4.4 wt%) than titanomagnetite (1.2 wt%) or magnetite (< 0.1 wt%). The high MnO content of ilmenite is attributed to retention of the pyrophanite ($MnTiO_3$) component in this phase as the ilmenite (*sensu stricto*) component is oxidized to form magnetite with increasing oxygen fugacity under magmatic conditions (Deer et al., 1992). All the reported hematite analyses contain high apparent SiO_2 concentrations (2.2–5.1 wt%), likely indicating the presence of impurities or inclusions in the analytical volumes.

5.8. Epidote and titanite

A small number of epidote and titanite analyses are given in Supplementary Table S8.

Epidote is an alteration product. Despite wide variation in composition and chemical formula, all the epidote analyses are rich in Al_2O_3, FeO and CaO with negligible amounts of MgO, MnO, TiO_2 and Na_2O.

Titanite is effectively pure stoichiometric $CaTiSiO_5$, except for the presence of Al_2O_3.

6. Geochemistry

Major, trace element and REE analyses of the WNMI uralitized gabbro are reported in Table 1 and can be compared to published data for the fresh appinitic gabbro of the same intrusion from Gahlan et al. (2018) and Samuel et al. (2015). The uralitized gabbro displays quite narrow range of SiO_2 contents (46.44–47.03 wt%). The uralitized

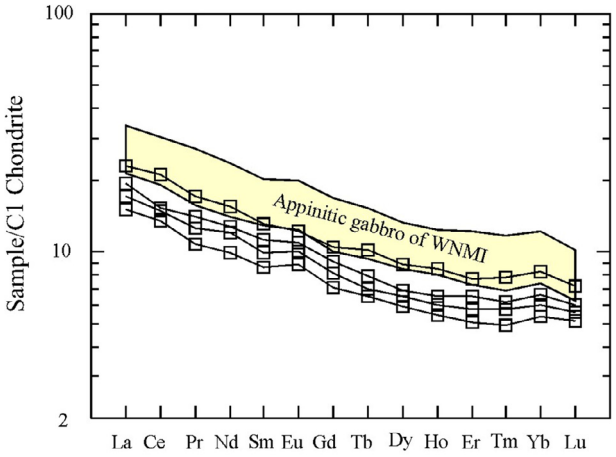

Fig. 4. Chondrite normalized REE patterns of the WNMI uralitized gabbro. Chondrite normalization values are from Evensen et al. (1978).

gabbro samples have higher LOI (3.41–3.68 wt%) than fresh gabbro (1.27–3.26 wt%, Gahlan et al., 2018), indicating substantial hydration during alteration. There are no clear differences in minor and trace element concentrations between the averages of fresh appinitic gabbro and uralitized gabbro with the exception of significantly higher Al_2O_3, CaO and LOI and lower LREE in the uralitized gabbro (Table 1).

REE analyses for four representative samples of the uralitized gabbro are given in Table 1. Chondrite-normalized REE patterns show subparallel trends (Fig. 4) with enrichment in LREE relative to the HREE [(La/Lu)n = 2.87–3.11] and essentially constant, slightly positive, Eu anomalies [(Eu/Eu* = 1.04–1.14). The REE patterns of the uralitized gabbro are parallel, but generally lower than the patterns of fresh samples of the intrusion (Gahlan et al., 2018).

7. Discussion

Prehnite occurs in a number of environments, associated with a range of rock types. It usually occurs: (1) as a late-stage phase formed during subsolidus cooling of igneous rocks, especially mafic volcanic rocks (e.g., Rose and Bird, 1987); (2) in hydrothermal alteration zones around the margins of granitic and mafic intrusions (e.g. Deer et al., 1965; Coleman, 1967; Cairncross et al., 2000); and (3) in low-grade metamorphic rocks (e.g. Coombs et al., 1959; Papeuk, 1974; Liou et al., 1983; Spaggiari, et al., 2002; Springer et al., 2007). Magmatic prehnite is generally considered impossible since the experiments of Coombs et al. (1959) and Liou (1971) show that prehnite is not stable above 450 °C. Field and petrographic evidence indicate that the WNMI is undeformed and the absence of any regional metamorphism in the area exclude a metamorphic origin for the prehnite in this locality.

The specific occurrence of prehnite in the uralitized gabbro at the margin of the WNMI and its absence in the mass of unaltered appinitic gabbro specifically indicate its formation during post-magmatic alteration processes. The cause of alteration was hydrothermal fluid circulation, likely of meteoric water driven by a magmatic heat source (although magmatic water derived directly from crystallizing granite is also possible), through the cooled and fractured appinitic gabbro forming the country rock of the granitic intrusions. Interaction between the appinitic gabbro of WNMI and later granitic intrusions resulted in a high degree of uralitization adjacent to the granite intrusions, decreasing with distance from the contacts. Hence, the formation of prehnite is linked to the process of uralitization, during which the alteration of pyroxene to secondary amphibole and of Ca-bearing plagioclase to albite releases the necessary CaO for the development of prehnite (e.g. Maggetti, 1972; Field and Rodwell, 1968; Coombs, 1954; Watson, 1953).

Textures and mineralogical compositions of the uralitized gabbro clearly indicate that the rock as a whole did not attain equilibrium during alteration; only local equilibria, at best, existed. Hence information is preserved, in the succession of minerals and their compositional changes, about both the magmatic origin and the alteration conditions experienced. Primary clinopyroxene, brown hornblende, dark brown biotite and Ca-rich plagioclase represent the magmatic assemblage of the appinitic gabbro. High Ti contents in brown hornblende and in dark brown biotite are indicators of high temperature of formation for these primary phases (e.g. Henry et al., 2005; Ridolfi et al., 2010).

We interpret the textural and compositional data in terms of a two-stage alteration process that transformed primary appinitic gabbro to uralitized gabbro. During the early stage, which we label “biotitization”, light brown to green biotite formed in the rock as fine aggregates or as parts of the decussate texture after hornblende. During this stage, actinolite and actinolitic hornblende with low Ti contents replaced clinopyroxene and primary amphibole. Moreover, the saussuritization of plagioclase and formation of titanite rims on ilmenite most probably accompanied this early stage of alteration. This whole stage is overprinted by the late stage of alteration, “chloritization”, characterized by partial replacement of all mafic minerals (including the products of first-stage alteration) by chlorite. The boundaries between chlorites and their mafic precursors (amphibole and biotite) are sharp, suggesting a rapid change of conditions.

Specific examination of the textures and compositions of prehnite support the inference of a two-stage hydrothermal alteration process. At least two generations of prehnite are evident in the petrography. The first generation formed either as a breakdown product of calcic plagioclase and amphibole—which can be nearly isochemical, *in situ* transformations with only local mass transport—or in intergrowths with biotite and pseudomorphs after pyroxene or plagioclase. The simultaneous formation of prehnite and secondary biotite calls for metasomatism or longer-range chemical exchange because no single parental mineral in the primary rock can decompose to prehnite plus biotite. The pseudomorphs indicate that saussuritization of plagioclase and uralitization of pyroxene yielded chemical components responsible for formation of the first generation of prehnite. On the other hand, the second generation of prehnite formed at the expense of early epidote and albite during the late, chlorite-forming stage of alteration. Fluid saturation at this stage is documented by the presence of late stage prehnite in veins and vug fillings.

The prehnite of late-stage textures, interstitial or in veins or vugs, can be found in some relatively unaltered gabbroic rocks of the WNMI alongside plagioclase and pyroxene preserved in early stages of partial saussuritization and uralitization. No locally-derived, first-stage prehnite is found within these samples. This prehnite was not formed by in-place replacement reactions; rather, these samples provide further evidence of fluid mobility during the late alteration stage, transporting components derived from the more heavily altered contact zone into the less altered inner margin of the intrusion. Such transport generally requires fractures to provide permeability and support infiltration of either magmatic water from the granitic intrusion or meteoric water circulation driven by the cooling of granite. Late-stage prehnite formation in less-altered gabbro hosts was likely concentrated along these precursor fractures.

8. Physicochemical conditions of the parent magma and alteration

The use of thermodynamic equilibrium among phases in the WNMI uralitized gabbro to assess conditions is problematic due to clear evidence of disequilibrium. The compositions of secondary minerals, particularly chlorite and actinolite, are controlled by the phases that they replace, suggesting that only very local equilibrium was attained and that distinct assemblages of alteration minerals may occur at the scale of individual thin sections. Nevertheless, compositions of

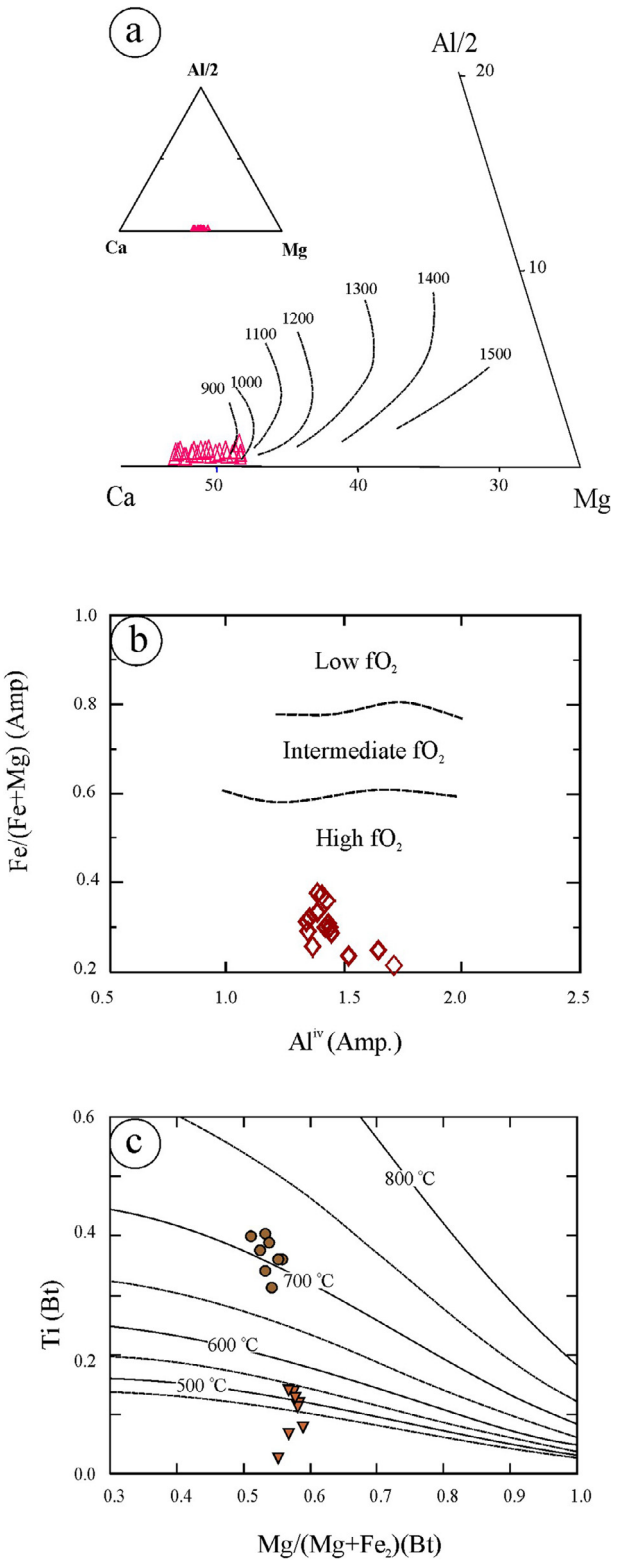

Fig. 5. (a) Ca-(Al/2)-Mg ternary diagram (after Nickel et al., 1985) for clinopyroxene. (b) Fe/(Fe + Mg) vs. Al^{IV} diagram for primary amphibole (Anderson and Smith, 1995). (c) Mg/(Mg + Fe) vs. Ti diagram of biotite with crystallization temperatures after Henry et al. (2005).

individual minerals, especially those that equilibrated at early, high-temperature stages, may provide constraints on the sources of fluids and the physicochemical conditions of fluid-rock interaction.

Mafic igneous minerals are, of course, sensitive to variations in both the chemistry and the P-T-a_{H2O}-f_{O2} conditions of crystallization, but a number of suitable assemblages enable quantitative P-T estimates (e.g., Lindsley, 1983; Nickel et al., 1985; Hammarstrom and Zen, 1986; Hollister et al., 1987; Blundy and Holland, 1990; Schmidt, 1992; Henry et al., 2005; Ridolfi et al., 2010). The quadrilateral diagram of Wo-En-Fs clinopyroxene compositions was contoured for temperature estimation by two-pyroxene thermometry by Lindsley (1983). Acknowledging that buffering of clinopyroxene composition by coexistence with amphibole is different from coexistence with orthopyroxene, we can nevertheless interpret the composition of fresh clinopyroxene relics as a lower bound on crystallization temperature because, at lower temperature, they would have exsolved orthopyroxene components either as a discrete phase or in a more complex reaction involving amphibole. The results are mainly between 800 and 1000 °C (Fig. 3a). The temperature contours in the Ca-Al/2-Mg diagram (Fig. 5a) of Nickel et al. (1985), which accounts for the influence of Al_2O_3 on two-pyroxene thermometry, likewise provide lower bound temperatures for homogeneous clinopyroxene relics below 900 °C.

Many authors have used the compositions of primary hornblende for geothermometry, oxybarometry, and especially geobarometry of plutonic rocks (Hammarstrom and Zen, 1986; Hollister et al., 1987; Blundy and Holland, 1990; Schmidt, 1992; Bachmann and Dungan, 2002; Ridolfi et al., 2008; Ridolfi et al., 2010). In the most recent thermobarometric formulation, Ridolfi et al. (2010) argue specifically that single-phase chemistry of amphibole yields reliable temperature and pressure estimates even without knowledge of coexisting or breakdown phase assemblages because amphiboles are typically perched at the limits of their stability. Application of the temperature-sensitive Si-index for amphibole from Ridolfi et al. (2010) retrieves crystallization temperature (with typical uncertainty of ± 22 °C) of primary hornblende between 865 and 925 °C. The textural interpretation of the appinitic gabbros (Gahlan et al., 2018), which suggests hornblende as the liquidus phase, followed by clinopyroxene, is generally consistent with the combined application of the Ridolfi et al. (2010) amphibole thermometer and the Nickel et al. (1985) clinopyroxene thermometer, whereas the older Lindsley (1983) pyroxene formulation (neglecting Al_2O_3) is inconsistent with this sequence for many samples.

The H_2O-pressure-sensitive total Al content of primary amphibole yields estimated confining pressure from 200 to 250 MPa, according to the formulation of Ridolfi et al. (2010). This pressure is only expected to agree with other Al-in-hornblende calibrations for the case of saturation with a pure H_2O fluid and hence is a lower bound on crystallization pressure. Calculated pressure of the primary amphiboles using the method of Schmidt (1992), on the other hand, ranges from 470 to 610 MPa with an average of 540 MPa. The oxygen-sensitive Fe/(Fe + Mg) versus Al^{IV} amphibole discrimination diagram (Anderson and Smith, 1995) shows that the primary amphiboles in the WNMI crystallized under high fO_2 conditions (Fig. 5b).

The concentration of Ti in biotite is very sensitive to temperature and fO_2, making it possible to use biotite to obtain temperature estimates for igneous and metamorphic rocks (Patiño Douce, 1993). Henry et al. (2005) used the binary diagram Ti versus Mg/(Mg + Fe) to calculate the crystallization temperatures of biotites. On this diagram (Fig. 5c), the primary biotite yields temperatures near 700 °C, while the secondary biotite gives much lower but also much more uncertain temperatures due to low and variable Ti content (all < 550 °C and many points < 450 °C). The low temperature estimates based on analysis of primary biotite are probably not accurate measurements of the crystallization temperature of igneous biotite. More likely they have been lowered by post-magmatic Fe-Mg exchange between biotite and other mafic minerals and represent closure temperatures for such Fe-Mg exchange. Nevertheless, the Ti contents, which are difficult to reset by diffusion, indicate, as would be expected, that primary biotite is a late magmatic phase, growing towards the end of the primary differentiation sequence of the gabbroic liquid, whereas secondary biotite is a

product of subsolidus alteration. The temperatures obtained here for secondary biotite are comparable to the range (300 to 500 °C) estimated for biotitization of primary igneous hornblende by Brimhall et al. (1985).

The observed compositions of chlorite depend, most probably, on the nature of their precursor ferromagnesian minerals and the conditions of alteration (temperature, composition, and redox state of aqueous solutions), as discussed by several investigators (e.g., Dodge, 1973; Eggleton and Banfield, 1985; Cathelineau, 1988; Bailey, 1988; Schneiderman, 1991; Abdel-Rahman, 1995). Nonetheless, an empirical chlorite geothermometer has been calibrated by Kranidiotis and MacLean (1987) for estimating the temperature of chlorite formation by replacement of mafic minerals. Calculated results from this formulation are less than 300 °C (Supplementary Table S6), consistent with the stability limits of chlorite and the petrographic evidence that chlorite formation happened at a later stage than biotite formation.

Finally, prehnite formation can be considered in light of the temperature sequence established by the other minerals from the primary and uralitized assemblages. The crystallization temperature of prehnite cannot exceed 450 °C, the homogeneous stability limit of the mineral (Coombs et al., 1959; Liou, 1971). Early-stage prehnite, accompanying biotitization, should therefore have formed between 300 and 450 °C. Hence the presence of prehnite provides a better upper bound on the first-stage alteration assemblage than the intergrown secondary biotite, whose nominal temperatures apparently scatter up to 550 °C. The late-stage prehnite associated with chlorite, on the other hand, should have formed below 300 °C. This is consistent with the experimental work of Liou et al. (1983), which showed prehnite growth at the expense of epidote at temperatures below 350 °C. The Fe^{3+}/Al^{3+} ratio of prehnite coexisting with epidote is a function of both f_{O2} and temperature (Liou et al., 1983) and these are difficult to separate from one another. Moreover, the sporadic occurrence of inconsistent f_{O2}-indicating minerals such as Mn-rich ilmenite, titanite and hematite in the uralitized gabbro suggests variable or poorly equilibrated f_{O2} during alteration (Kay, 1983).

9. Conclusions

- Prehnite-bearing assemblages were found in and near uralizited gabbro formed at the margins of late Neoproterozoic WNMI in south Sinai, which were driven by intense hydrothermal alteration at the margins of the pluton during intrusion of younger granites.
- Two stages of mineral replacement are evident. The early stage includes uralitization of pyroxene, formation of new biotite as aggregates of small flakes, transformation of primary amphiboles into actinolite and actinolitic hornblende and saussuritization of plagioclase. The late stage of alteration is characterized by chloritization of mafic minerals.
- Prehnite forms (1) fine grained aggregates replacing the feldspars and amphiboles, (2) prehnite-biotite intergrowths and (3) small veinlets and vug fillings associated with other alteration products. The first two listed forms are associated with the first stage of alteration. The third form is associated with the late, chlorite-forming stage, wherein prehnite formed at expense of early epidote.
- Mineral chemistry and stability constraints along with petrographic relations establish a temperature sequence from liquidus hornblende growth at 865–925 °C, through near-liquidus primary clinopyroxene crystallization above 800 °C to near-solidus primary biotite growth, followed by the early prehnite and biotite-forming stage of alteration at moderate temperature (300–450 °C) and finally the late chlorite-forming stage of alteration at low temperature (< 300 °C).

Acknowledgements

The authors are indebted to King Saud University, Deanship of Scientific Research, Research Group No. (RG-1436-036). Chi Ma is thanked for assistance with electron microprobe analyses at Caltech. PDA's participation was supported by NSF geo-informatics award EAR-1550934.

Appendix A. Supplementary material

Supplementary data associated with this article can be found, in the online version, at https://doi.org/10.1016/j.jseaes.2018.04.011.

References

Abdel-Karim, A.M., 2013. Petrology, geochemistry and petrogenetic aspects of younger gabbros from south Sinai: a transition from arc to active continental margin. Chemie der Erde 73, 89–104.
Abdel-Rahman, A.M., 1995. Chlorites in a spectrum of igneous rocks: mineral chemistry and paragenesis. Mineral. Mag. 59, 129–141.
Anderson, J.L., Smith, D.R., 1995. The effects of temperature and fO2 on the Al-in-hornblende barometer. Am. Mineral. 80, 549–559.
Azer, M.K., 2007. Tectonic significance of Late Precambrian calc-alkaline and alkaline magmatism in Saint Katherina area, South Sinai, Egypt. Geologica Acta 5 (3), 255–272.
Azer, M.K., Abu El-Ela, F.F., Ren, M., 2012. The petrogenesis of late Neoproterozoic mafic dyke-like intrusion in south Sinai. Egypt. J. Asian Earth Sci. 54–55, 91–109.
Azer, M.K., El-Gharbawy, R.I., 2011. Contribution to the Neoproterozoic layered mafic-ultramafic intrusion of Gabal Imleih, south Sinai, Egypt: implication of post-collisional magmatism in the north Arabian-Nubian Shield. J. Afr. Earth Sc. 60, 253–272.
Azer, M.K., Obeid, M.A., Gahlan, H.A., 2016. Late Neoproterozoic layered mafic intrusion of arc-affinity in the Arabian-Nubian Shield: a case study from the Shahira layered mafic intrusion, southern Sinai, Egypt. Geologica Acta 14, 237–259.
Bachmann, O., Dungan, M., 2002. Temperature-induced Al-zoning in hornblendes of the Fish Canyon magma, Colorado. American Mineralogist 87, 1062–1076.
Bailey, S.W., 1988. Chlorites: Structures and crystal chemistry. Rev. Mineral. 19, 347–398.
Basta, E.Z., 1960. Natural and synthetic titano-magnetite (the system Fe_2O_3-Fe_2TiO_4-$FeTiO_3$). N. Jb. Min. Abh. 94, 1017–1048.
Be'eri-Shlevin, Y., Katzir, Y., Whitehouse, M., 2009. Post-collisional tectono-magmatic evolution in the northern Arabian-Nubian Shield (ANS): time constraints from ion-probe U-Pb dating of zircon. J. Geol. Soc. 166, 71–85.
Be'eri-Shlevin, Y., Samuel, M.D., Azer, M.K., Rämö, O.T., Whitehouse, M.J., Moussa, H.E., 2011. The Ediacaran Ferani and Rutig volcano-sedimentary successions of the northernmost Arabian-Nubian Shield (ANS): New insights from zircon U-Pb geochronology, geochemistry and O–Nd isotope ratios. Precambr. Res. 188, 21–44.
Bettison, L.A., Schiffman, P., 1988. Compositional and structural variations of phyllosilicates from the Point Sal ophiolite, California. Am. Mineral. 73, 62–76.
Blundy, T.D., Holland, T.J.B., 1990. Calcic amphibole equilibria and a new amphibole-plagioclase geothermometer. Contrib. Mineral. Petrol. 104, 208–224.
Brimhall, G., Agee, C., Stoffregen, R., 1985. The hydrothermal conversion of hornblende to biotite. Can. Mineral. 23, 369–379.
Buddington, A.F., Lindsley, D.H., 1964. Iron-titanium oxide minerals and synthetic equivalents. J. Petrol. 5, 310–357.
Cairncross, B., Tsikos, H., Harris, C., 2000. Prehnite from the Kalahari manganese field, South Africa, and its possible implications. S. Afr. J. Geol. 103 (3–4), 231–236.
Cathelineau, M., 1988. Cation site occupancy in chlorites and illites as a function of temperature. Clay Miner. 23, 471–485.
Coleman, R.G., 1967. Low-temperature reaction zones and alpine ultramafic rocks of California, Oregon, and Washington. United State Geological Survey Bulletin, 1247, 49p.
Coombs, D.S., 1954. The nature and alteration of some Triassic sediments from Southland, New Zealand. Trans. Roy. Soc. N.Z. 82, 65–109.
Coombs, D.S., Bills, A.J., Fyfe, W.S., Taylor, A.M., 1959. The zeolite fades; with comments on the interpretation of hydrothermal syntheses. Geochimica et Cosmochimica Acta 17, 53–107.
Deer, W.A., Howie, B.A., Zussman, J., 1965. Rock-forming Minerals Volume 3, Sheet Silicates: London, Longmans, Green, and Co., 270p.
Deer, W.A., Howie, R.A., Zussman, J., 1992. An Introduction to the Rock Forming Minerals, second ed. Longman Scientific and Technical, London, pp. 696.
Dodge, F.C.W., 1973. Chlorites from granitic rocks of the central Sierra Nevada batholith, California. Mineral. Mag. 39, 58–64.
Eggleton, R.A., Banfield, J.F., 1985. The alteration of granitic biotite to chlorite. Am. Mineral. 70, 902–910.
Essawy, M.A., Hassan, M.A., 1977. The occurrence of Prehnite in Uralitized Gabbros from Egypt. Verh. Geol. B.A.S. 405–406.
Evensen, N.M., Hamilton, P.J., O' Nions, R.K., 1978. Rare earth abundances in chondritic meteorites. Geochimica et Cosmochimica Acta 42, 1199–1212.
Eyal, M., Bentor, Y.K., Goor A., Bruner, I., Eyal, Y., Calvo, R., Hall, J.K., and Rosensaft, M., 2013. Geological map of Katherina ring complex, Sinai, Egypt. Geological Survey of Israel, Scale 1:50,000, sheet 1.
Field, D., Rodwell, J.B., 1968. The occurrence of prehnite in a high grade metamorphic sequence from south Norway. Norsk Geologisk Tidsskrift 48, 55–59.
Gahlan, H.A., Obeid, M.A., Azer, M.K., Asimow, P.D., 2018. An example of post-collisional appinitic magmatism with an arc-like signature: the Wadi Nasb mafic intrusion, north Arabian-Nubian Shield, south Sinai, Egypt. Int. Geol. Rev. 60, 865–888.

Hammarstrom, J.M., Zen, E.-An., 1986. Aluminium in hornblende: an empirical igneous geobarometer. Am. Mineral. 71, 1297–1313.
Henry, D.J., Guidotti, C.V., Thomson, J.A., 2005. The Ti-saturation surface for low-to-medium pressure metapelitic biotites: implications for geothermometry and Ti substitution mechanisms. Am. Mineral. 90, 316–328.
Hey, M.H., 1954. A new review of the chlorites. Mineral. Mag. 30, 272–292.
Hollister, L.S., Grissom, G.C., Peters, E.K., Stowell, H.H., Sisson, V.B., 1987. Confirmation of the empirical correlation of Al in hornblende with pressure of solidification of calc-alkaline plutons. Am. Mineral. 72, 231–239.
Kay, S.M., 1983. Metamorphism in the Aleutian arc: the finger bay pluton, Adak, Alaska. Can. Mineral. 2l, 665–681.
Keeditse, M., Rajesh, H.M., Belyanin, G.A., Fukuyama, M., Tsunogae, 2016. Primary magmatic amphibole in Archaean meta-pyroxenite from the central zone of the Limpopo Complex, South Africa. S. Afr. J. Geol. 119 (4), 607–622.
Khalil, A.E.S., Obeid, M.A., Azer, M.K., 2015. Late Neoproterozoic post-collisional mafic magmatism in the Arabian-Nubian Shield: a case study from Wadi El-Mahash gabbroic intrusion in southeast Sinai, Egypt. J. Afr. Earth Sci. 105, 29–46.
Kranidiotis, P., MacLean, W.H., 1987. Systematics of chlorite alteration at the Phelps Dodge massive sulfide deposit, Matagami, Quebec. Econ. Geol. 82, 1898–1911.
Leake, B.E., Woolley, A.R., Arps, C.E.S., Birch, W.D., Gilbert, M.C., Grice, J.D., Hawthorne, F.C., Kato, A., Kisch, H.J., Krivovichev, V.G., Linthout, K., Laird, J., Mandarino, J., Maresch, W.V., Nickel, E.H., Rock, N.M.S., Schumacher, J.C., Smith, D.C., Stephenson, N.C.N., Ungaretti, L., Whittaker, E.J.W., Youzhi, V., 1997. Nomenclature of amphiboles: report of the subcommittee on amphiboles of the international mineralogical association commission on new minerals and mineral names. Mineral. Mag. 61, 295–321.
Le Bas, M.J., 1962. The role of aluminum in igneous clinopyroxenes with relation to their parentage. Am. J. Sci. 260, 267–288.
Lindsley, D.H., 1983. Pyroxene thermometry. Am. Mineral. 68, 477–493.
Liou, J.G., 1971. Synthesis and stability relations of prehnite, $Ca_2Al_2Si_3O_{10}(OH)_2$. Am. Mineral. 57, 507–531.
Liou, J.G., Kim, H.S., Maruyama, S., 1983. Prehnite – epidote equilibria and their petrologic applications. J. Petrol. 24 (4), 321–342.
Maggetti, M., 1972. Prehnite in basic plutonic rocks from the Odenwald (Germany). Neues Jahrbuch für Mineralogie – Monatshefte 6, 241–246.
Matsueda, M., 1975. Iron-rich prehnite from the skarn of Sampo mine, Okayama Prefecture, Japan. (in Japanese) Sci. Rept. Dept. Geol. Kyushu University, Fukuoka, vol. 12, pp. 91–100.
Mehanna, A.M., Wetait, M.A., El-Amawy, M.A., Solimani, F.A., Ghabour, Y., 2004. Petrogenesis and metamorphism of the basement rocks of Imlig area, southwest Sinai, Egypt. Ann. Geol. Survey Egypt XXVII, 35–59.
Moreno, J.A., Montero, P., Abu Anbar, M., Molina, J.F., Scarrow, J.H., Talavera, C., Cambeses, A., Bea, F., 2012. SHRIMP U-Pb zircon dating of the Katerina Ring Complex: Insights into the temporal sequence of Ediacaran calc-alkaline to peralkaline magmatism in southern Sinai, Egypt. Gondwana Res. 12, 887–900.
Morimoto, N., Fabries, J., Ferguson, A.K., Ginzburg, I.V., Ross, M., Seifert, F.A., Zussman, J., 1988. Nomenclature of pyroxenes: Mineralogical Magazine 52, 535–550.
Moussa, H.E., 1999. Mineral chemistry and petrochemistry of amphibolite from Taba area, NE Sinai. Egypt. Mineral. 11, 187–210.
Nachit, H., Ibhi, A., Abia, E.H., Ohoud, M.B., 2005. Discrimination between primary magmatic biotites, reequilibrated biotites and neoformed biotites. Comptes Rendus Géoscience 337, 1415–1420.
Nickel, K.G., Brey, G.P., Kogarko, L., 1985. Orthopyroxene-clinopyroxene equilibria in the system CaO-MgO-Al_2O_3-SiO_2 (CMAS): new experimental results and implications for two-pyroxene thermometry. Contrib. Miner. Petrol. 91, 44–53.
Papeuk, S.P., 1974. Prehnite-pumpellyite facies metamorphism of late Precambrian rocks of the Avalon Peninsula. Can. Mineral. 12, 463–468.
Patiño Douce, A.E., 1993. Titanium substitution in biotite: an empirical model with applications to thermometry, O_2 and H_2O barometries, and consequences form biotite stability. Chem. Geol. 108, 133–162.
Ridolfi, F., Puerini, M., Renzulli, A., Menna, M., Toulkeridis, T., 2008. The magmatic feeding system of El Reventador volcano (Sub-Andean zone, Ecuador) constrained by texture, mineralogy and thermobarometry of the 2002 erupted products. J. Volcanol. Geoth. Res. 176, 94–106.
Ridolfi, F., Renzulli, A., Puerini, M., 2010. Stability and chemical equilibrium of amphibole in calc-alkaline magmas: an overview, new thermobarometric formulations and application to subduction-related volcanoes. Contrib. Miner. Petrol. 160, 45–66.
Rose, N.M., Bird, D.K., 1987. Prehnite-epidote phase relations in the Nordre Aputitëq and Kruuse Fjord layered gabbros, East Greenland. J. Petrol. 28 (6), 1193–1218.
Samuel, M.D., Ghabrial, D.S., Moussa, H.E., Ali-Bik, M.W., 2015. The petrogenesis of late Neoproterozoic gabbro/diorite intrusion at Sheikh El-Arab area, central Sinai, Egypt. Arab. J. Geosci. 8 (8), 5579–5599.
Schmidt, M.W., 1992. Amphibole composition in tonalite as a function of pressure: an experimental calibration of the Al-in hornblende barometer. Contrib. Mineral. Petrol. 110, 304–310.
Schneiderman, J.S., 1991. Petrology and mineral chemistry of the Ascutney Mountain igneous complex. Am. Mineral. 76, 218–229.
Soliman, F., 1996. Geology of Wadi Tarfa-Wadi Isla region, southern Sinai, Egypt. Middle East Research Center, Ain Shams University. Earth Sci. Ser. 10, 214–228.
Spaggiari, C.V., Gray, D.R., Foster, D.A., 2002. Blueschist metamorphism during accretion in the Lachlan Orogen, south-eastern Australia. J. Metamorph. Petrol. 20 (8), 711–726.
Springer, R.K., Day, H.W., Beiersdorfer, R.E., 2007. Prehnite-pumpellyite to greenschist facies transition, Smartville Complex, near Auburn, California. J. Metamorph. Geol. 10 (2), 147–170.
Watson, K.D., 1953. Prehnitization of albitite. Am. Mineral. 38, 197–207.